3D bioprinting of high-performance hydrogel with in-situ birth of stem cell spheroids

Shunyao Zhu [a], Xueyuan Liao [a], Yue Xu [a], Nazi Zhou [a], Yingzi Pan [a], Jinlin Song [b], Taijing Zheng [a], Lin Zhang [a], Liyun Bai [a], Yu Wang [a], Xia Zhou [a,c], Maling Gou [d], Jie Tao [a,**], Rui Liu [a,*]

[a] *Department of Stomatology, Daping Hospital, Army Medical University (The Third Military Medical University), Chongqing, 400042, China*
[b] *College of Stomatology, Chongqing Medical University, Chongqing, China*
[c] *State Key Laboratory of Trauma, Burn and Combined Injury, Third Military Medical University, Chongqing, 400042, China*
[d] *State Key Laboratory of Biotherapy and Cancer Center, West China Hospital, Sichuan University, and Collaborative Innovation Center for Biotherapy, Chengdu, Sichuan, 610065, China*

ARTICLE INFO

ABSTRACT

Digital light processing (DLP)-based bioprinting technology holds immense promise for the advancement of hydrogel constructs in biomedical applications. However, creating high-performance hydrogel constructs with this method is still a challenge, as it requires balancing the physicochemical properties of the matrix while also retaining the cellular activity of the encapsulated cells. Herein, we propose a facile and practical strategy for the 3D bioprinting of high-performance hydrogel constructs through the in-situ birth of stem cell spheroids. The strategy is achieved by loading the cell/dextran microdroplets within gelatin methacryloyl (GelMA) emulsion, where dextran functions as a decoy to capture and aggregate the cells for bioprinting while GelMA enables the mechanical support without losing the structural complexity and fidelity. Post-bioprinting, the leaching of dextran results in a smooth curved surface that promotes in-situ birth of spheroids within hydrogel constructs. This process significant enhances differentiation potential of encapsulated stem cells. As a proof-of-concept, we encapsulate dental pulp stem cells (DPSCs) within hydrogel constructs, showcasing their regenerative capabilities in dentin and neovascular-like structures *in vivo*. The strategy in our study enables high-performance hydrogel tissue construct fabrication with DLP-based bioprinting, which is anticipated to pave a promising way for diverse biomedical applications.

1. Introduction

Owing to the superior performance in both printing resolution and speed, digital light processing (DLP)-based 3D bioprinting technology has emerged as a powerful tool to fabricate hydrogel constructs for tissue engineering and regenerative medicine [1,2]. Compared to classical extrusion-based bioprinting technologies, this advanced technology can continuously lift the products by using polydimethylsiloxane (PDMS) substrate to avoid interfacial defects and improve the structural integrity [3]. Over the past decade, an array of both synthetic and natural materials has been extensively investigated for their suitability in DLP-based bioprinting of hydrogel constructs, aiming to guide cell functions effectively [4,5]. Particularly, loading stem cells into 3D-bioprinted hydrogel constructs has received increasing attention [6]. After tissue constructs accomplishment, the constructed matrix preserves the encapsulated cells by providing biochemical/biophysical cues (e.g., geometric structure, viscosity, and adhesion), while the encapsulated mesenchymal stem cells (MSCs) can differentiate into host cells or regulate the microenvironment by paracrine *in vitro* and *in vivo* [7]. Despite these advancements, there are still challenges to be surmounted in the development of bioinks that possess the ideal balance of printability, mechanical strength, and structural stability, without compromising the bioactivity of the encapsulated stem cells [8,9].

Stem cell spheroids, which are three-dimensional, spherical clusters

---

of cells, have been shown to effectively replicate *in vivo* conditions, including intricate cell-cell and cell-extracellular matrix (ECM) interactions. These spheroids exhibit an elevated resistance to apoptosis, which equips them to better withstand the challenges of the wound healing microenvironment [10,11]. With their unique attributes of self-renewal, maintenance of stemness, and protein secretion, these spheroids have been shown in numerous studies to direct the specific functions and growth of cells in the context of tissue engineering and regenerative medicine [12,13]. Consequently, the incorporation of stem cell spheroids into 3D bioprinted hydrogels is gaining significant attention for its potential to replicate physiological microenvironments and to enhance therapeutic outcomes with added flexibility [14]. Andrew C. Daly et al. proposed an extrusion-based bioprinting strategy

[15] to transfer the pre-prepared spheroids into self-healing supporting hydrogels, replicating the features of scarred cardiac tissues. However, this method constructs 3D structures drop-by-drop, using spheroids as fundamental building blocks, which can be time-consuming when fabricating large, centimeter-scale tissue models. Additionally, the printing resolution is constrained by the physical dimensions of the transferred spheroids. More importantly, the aggregation of cells results in a higher sedimentation coefficient [16], which poses challenges for DLP-based bioprinting with low-viscosity bioinks (ranging from 0.25 to 10 Pas) [17]. Therefore, overcoming these limitations of DLP-based bioprinting is of paramount importance to pave the way for the successful creation of structurally and physiologically relevant biofabricated constructs.
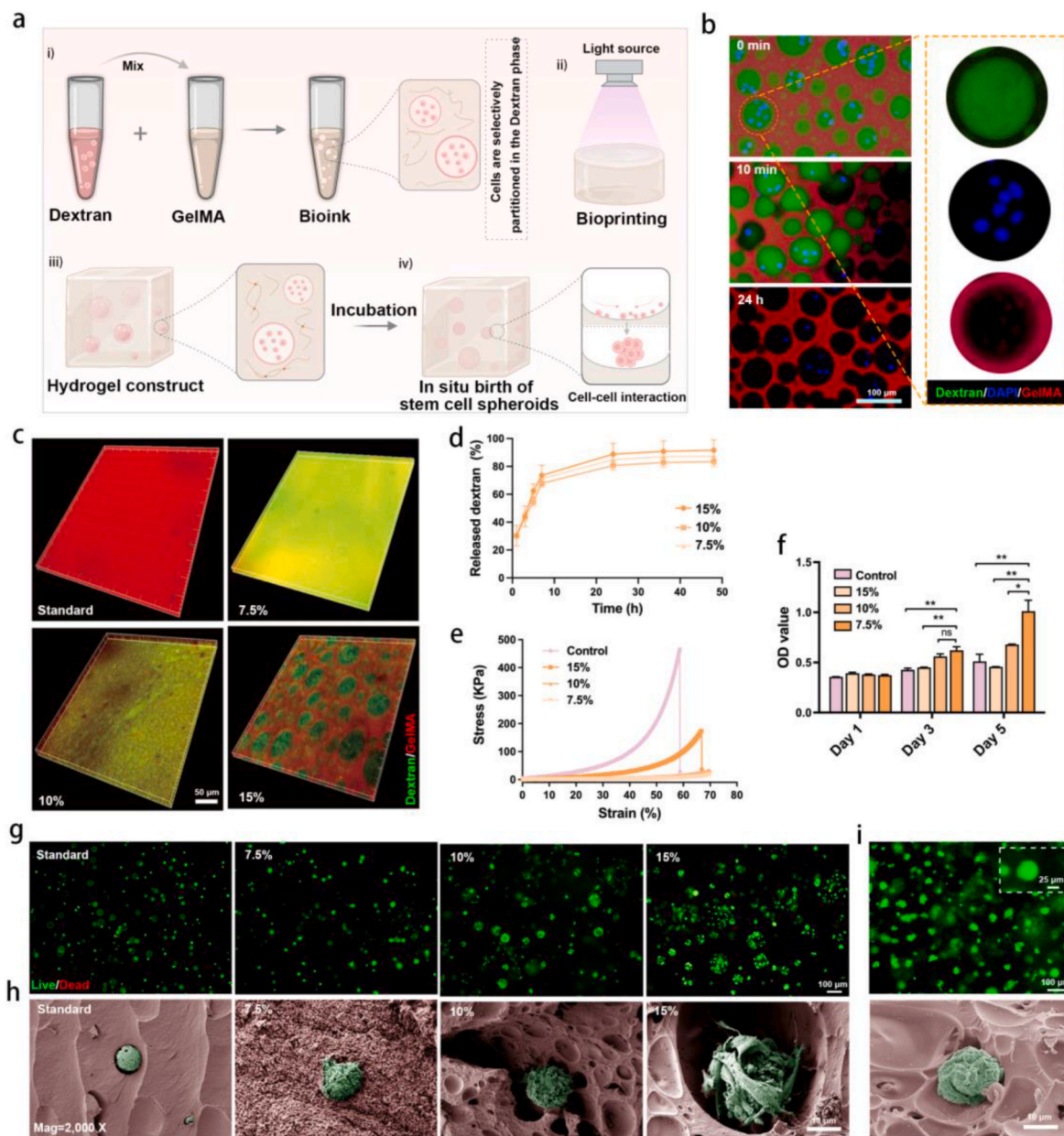
Fig. 1. Characterizations of the bioink. (a) Schematic representation of the bioink used for DLP-based bioprinting and its application in facilitating in situ birth of stem cell spheroids. (b) Cell distribution and dextran removal process within hydrogels. (c) Visualization of different GelMA concentration with dextran at a volume ratio of 2:1 on the distribution of dextran. (d) The profile of released dextran. (e) The representative compressive stress-strain curve of the hydrogels. (f) Quantitative cell proliferation results of NIH/3T3 at day 1, 3 and 5 (mean ± SD, n = 3, two-way ANOVA). (g) Representative live/dead images of the NIH/3T3 cells at day 5. Live cells were stained in green, while dead cells were stained in red. (h) SEM micrographs of NIH/3T3 cells within hydrogel at day 5 cultured. (i) Representative live/dead and SEM images of the BMSCs in CCB group of 15 %. Ns was determined as $P > 0.05$ with no statistical difference, $*P < 0.05$, $**P < 0.01$.

In-situ birth of spheroids within the hydrogels has attracted much attention to address above limitations. Hydrogels with anti-adhesive properties can resist protein adsorption through the retention of water molecules on the hydrophilic surface, resulting in the aggregation of seeded stem cells [18]. Meanwhile, the porous structure can also aid the stem cell spheroids formation owing to the geometric signals. Kunxi Zhang [19] et al. engineered a porous hydrogel made from amide-bonded poly(L-glutamic acid) and chitosan, designed to support adipose stem cell (ASC) spheroids for cartilage regeneration. Yet, porous structure generation process that combines air-drying and freeze-drying is not ideal to be applied in a DLP-based bioprinting platform, as it is not possible to encapsulate any live cells during the fabrication of these hydrogels. Moreover, when cells are loaded into pre-prepared scaffolds, a non-uniform cell distribution can occur. Recently, a new strategy of coacervation to drive the phase separation and pore formation was proposed via inducing the supramolecular assemblies into poly(vinyl alcohol) (PVA) solution [20]. This approach had been shown to create porous hydrogels that better supported the in-situ growth of encapsulated stem cell spheroids. However, the cells were initially distributed evenly throughout the pre-polymer solution, and only a portion of them ended up in the pores after coacervation. Furthermore, the use of synthetic polymers as the hydrogel matrix may limit biomedical applications due to concerns regarding biodegradation and tissue integration.

In this work, to drive stem cell spheroids formation within printed hydrogel in situ, we proposed an anisotropic bioink with dextran as a cell decoy to capture encapsulated stem cells and GelMA as matrix to provide structural support, thus facilitating bioprinting of high-performance hydrogel tissue constructs (Fig. 1a). The bioink formulation demonstrated enhanced cell viability post-printing without compromising the precision required for constructing intricate 3D architectures. Notably, we found that our proposed strategy enabled MSC spheroid growth after bioprinting, resulting in significant up-regulation of stemness maintenance and differentiation potential. Concurrently, our finding indicated that this method effectively promoted the development of a vascular network within hydrogels. Further validation was provided by a rat subcutaneous implant model, where the hydrogel, enriched with dental pulp stem cells (DPSCs), demonstrated its capacity to support the regenerative dentin and neovascular-like structures *in vivo*.

2. Materials and methods

2.1. Materials

Materials included gelatin (Sigma Aldrich), methacrylic anhydride (Sigma Aldrich), sodium carbonate (Aladdin), sodium bicarbonate (Aladdin), Cell Counting Kit-8 (CCK-8, MCE), Live/Dead (KeyGEN BioTECH), poly (ethylene oxide) (PEO, Sigma), 4',6-diamidino-2-phenylindole (DAPI, Thermo Fisher), FITC-labeled dextran (average Mw = 500000, Sigma), dextran (average Mw = 500000, Sigma) and lithium phenyl-2,4,6-trimethyl-benzoylphosphinate (LAP, bidepharm).

All animals were purchased from Beijing HFK Bio-Technology.co and were acclimatized to the environment of the animal facility for at least 7 d prior to the experiments. All of the animals and related procedures were performed according to the standard guidelines approved by the ethics committee of Army Medical University (AMUWEC20212172) and complied with the guidelines of the National Institutes of Health Guide for Care and Use of Laboratory Animals.

2.2. Preparation and characterization of the bioink

Gelatin methacryloyl (GleMA) was synthesized according to our previous study [21]. To fabricate the bioink, GelMA solution and dextran solution were prepared prior to cell encapsulation. Briefly, lyophilized GleMA was dissolved in PBS solution containing 0.5 % (w/v) of LAP (photoinitiator) to reach a final concentration of 15 %, 10 % and

7.5 %(w/v). Dextran powder was dissolved into the PBS solution with a final concentration of 10 %. All the solutions were sterilized with syringe filters (0.22 μm). GelMA solution was mixed with dextran solution by pipetting. The morphology of the emulsion was imaged using a microscope and dextran microdroplet size was analyzed by ImageJ software.

To visualize the morphology of the porous structure, GelMA conjugated with rhodamine B and dextran conjugated with FITC were used and imaged by using a confocal fluorescence microscope (Leica SP7, Germany). Compression properties of the hydrogels were measured using a mechanical testing machine at room temperature (ElectroForce 400N, TA).

To investigate the swelling ratio of the printed hydrogels, the mass of each hydrogel was measured at different time. The swelling ratio was determined as a percentage using the following formula:

$$swelling\ ratio = \frac{w_t}{w_0} \times 100\%$$

where W_t is the swollen hydrogel weight and W_0 is the initial prepared hydrogel weight.

2.3. In vitro and in vivo degradation of the hydrogel constructs

For the *in vitro* degradation assessment, we employed rhodamine-labeled GelMA to track the degradation process. The cylindrical hydrogels were meticulously bioprinted and then placed into a collagenase solution for incubation. At predetermined time intervals, images documenting the degradation of the hydrogels were captured. To quantitatively analyze the degradation, Image J software was utilized to perform a comprehensive statistical analysis. This analysis focused on the fluorescence intensity and the area of the degraded regions, providing a robust dataset to evaluate the degradation kinetics and the structural integrity of the bioprinted constructs over time.

A hydrogel construct, measuring 5 mm in diameter and 2 mm in height, was meticulously bioprinted and then subcutaneously implanted into a mouse model. Tissue samples were meticulously harvested at specific postoperative time points: the 7th, 14th, and 28th days. Initially, the collected samples were fixed in a 4 % paraformaldehyde solution for a duration of 48 h to preserve their structural integrity. Subsequently, hematoxylin and eosin (H&E) staining was conducted to assess tissue infiltration and to scrutinize the degradation patterns of the hydrogel. This staining technique allowed for the visualization of cellular structures and the evaluation of the hydrogel's interaction with the surrounding tissue environment, providing valuable insights into the biocompatibility and degradation profile of the implanted hydrogel.

2.4. 3D bioprinting of hydrogel constructs

The bioprinting process was facilitated by a digital light processing (DLP)-based 3D printing system, which comprised a digital micromirror device (DMD) chip, a motion controller-operated movable stage, a light source, a printing stage, and a computer equipped with software to orchestrate the system's components. The motion controller and stage worked in tandem to meticulously regulate the thickness of the printed samples. Multi-material printing was accomplished by manually swapping the bath solution. The 3D molds were meticulously designed using SolidWorks software and then sliced with 3D Slicer software. The resulting images were sequentially loaded onto the DMD chip. During each printing step, bioink was manually applied to the stage using a pipette and exposed to light for polymerization. To prevent cross-contamination, the ink on the printing platform was replaced, and the sample was thoroughly rinsed with warm PBS after each section was printed. By iterating these steps, a 3D construct was successfully fabricated. The bioprinted hydrogel constructs were then immersed in warm PBS to eliminate any uncrosslinked polymers and photoinitiators. In the DLP 3D bioprinter, the printing parameters were meticulously set as

follows: a light wavelength of 405 nm, a light intensity of 60 mW/cm^2, a Z-axis speed of 0.1 mm/s, and a curing time of 10 s for each layer.

2.5. Isolation and culture of cells

Briefly, dental pulp was extracted from the lower incisors of 4-week-old male Sprague-Dawley (SD) rats, then cut into pieces of less than 1 mm in 0.01 M PBS and digested with type I collagenase (3 mg/mL, Sigma Aldrich) and dispase (3 mg/mL, Beyotime) for 60 min (37 °C). Digestion was neutralized with α-MEM medium containing 10 % fetal bovine serum (FBS, Gibco), 0.292 mg/mL glutamine (Invitrogen), 100 units/mL penicillin (Gibco), 100 mg/mL streptomycin (Gibco). After filtration, rat dental pulp stem cells (rDPSCs) were harvested and plated in 25 cm^2 culture flasks (Costar) with complete medium.

Bone marrow derived mesenchymal stem cells (BMSCs) were isolated from rat femur and tibia as described previously [22]. Cells were used in the 3rd or 4th passage. Human umbilical vein endothelial cells (HUVECs) and human DPSC (hDPSC) were purchased from MeisenCTCC and cultured in EGM-2 medium (Lonza) for HUVEC and α-MEM (BI) + 10 % FBS (Gibco) + 100 U/100 μg/mL Pen/Strep for hDPSC. Cells were used in the 3rd or 4th passage. NIH/3T3 cells were purchased from Procell and cultured in high-glucose DMEM medium with 10 % FBS (Gibco), and 1 % penicillin/streptomycin at 37 °C under 5 % CO$_2$. Culture was maintained following the supplier's protocols.

2.6. Cell-laden hydrogel preparation and characterization

Cells were trypsinized and re-suspended in dextran solution to form the cell suspension. Then, the cell suspension dropped into the GelMA solution following exposure to light (405 nm). The cell directly resuspended in pure GelMA solution was treated as the standard GelMA group. The cell-laden hydrogel constructs were immersed into medium to remove the LAP and were cultured in standard cell culture condition (37 °C and 5 % CO$_2$).

Meanwhile, we prepared a GelMA/PEO emulsion bioink as a control group. Cells were trypsinized and re-suspended in PEO solution (1.6 %, w/v) to form the cell suspension. Then, the cell suspension dropped into the GelMA solution (15 %, w/v) at a volume ratio of 1:2 following exposure to light. The cell distribution was calculated with Image J software.

Viability of cells within the hydrogel was investigated by a Live/dead assay. Images were captured by an inverted fluorescence microscope. Live cells were stained in green, while dead cells were stained in red. CCK-8 was used to quantitatively evaluate the proliferation of encapsulated cells. The cytoskeleton was stained with Alexa 488-phalloidin and nucleus was stained with DAPI. Meanwhile, micromorphology of encapsulated cells was evaluated using scanning electron microscopy (SEM, FEI, Netherlands).

2.7. Histological evaluation

For H&E and Masson's Trichrome staining, the constructs were fixed in 4 % paraformaldehyde for more than 24 h. After washing with PBS, the fixed samples were placed in gradient ethanol solution for dehydration, followed by a conventional paraffin-embedding protocol. The sections were immersed in xylene for deparaffinization and then placed in decreasing concentrations of ethanol for rehydration. Samples were stained with H&E and Masson's Trichrome using standard protocols.

The harvested samples were fixed in 4 % paraformaldehyde, processed, embedded, and sectioned for immunostaining. The primary antibodies were anti-SOX2 (1:200, GeneTex, Cat. No. GTX101507, USA); anti-OCT4 (1:200, GeneTex, Cat. No. GTX101497, USA); anti-NANOG (1:200, Novus, Cat. No. abs131488, USA); anti-CD31 (1:200, Santa Cruz, Cat. No. sc-376764, USA); anti-human CD31) (1:1000, Abcam, Cat. No. ab9498, UK); anti-DSPP (1:100, Santa Cruz, Cat. No. sc-73632, USA); anti-NF200 (1:500, Servicebio, Cat. No. GB12144, China). The

secondary antibodies were Goat anti-rabbit lg-G TRITC (Beijing Zhong Shan-Golden Bridge, Cat. No. ZF-0316, China), goat anti-mouse Ig-G TRITC (Beijing Zhong Shan-Golden Bridge, Cat. No. ZF-0301, China), and goat anti-rabbit Ig-G (Beijing Zhong Shan-Golden Bridge, Cat. No. PV-9001, China). Next, samples were incubated with 50 μg/mL DAPI to stain the nucleus for immunofluorescence, or stained nuclei with hematoxylin after diaminobenzidine (DAB) staining for immunohistochemical. All samples were examined under a microscope (OLYMPUS, Japan).

2.8. In vitro multilineage differentiation

To induce osteogenic differentiation, the hydrogel constructs were incubated in a basal medium containing dexamethasone (100 nM), L-ascorbic acid (50 μM), and β-glycerophosphate (10 mM) osteogenic supplement medium. The medium was changed every 2–3 days, and cultured for 21 days. Related gene expression was determined by Real-Time polymerase chain reaction (qRT-PCR). To evaluate the degree of mineralization, the osteogenic cells were washed with PBS solution, fixed with 4 % paraformaldehyde, and then stained with Alizarin Red S solution. The samples were then rinsed with distilled water for three times.

To induce adipogenic differentiation, cell-laden hydrogel constructs were cultured in a basal medium containing dexamethasone (1 μM), indomethacin (200 μM), insulin (10 μM), 3-isobutyl-1-methylxanthin (IBMX, 500 μM) adipogenic supplement medium for 21 days. The samples were stained with Oil Red O to assess the degree of adipogenic differentiation. After fixed with 4 % paraformaldehyde, the samples were washed with 60 % isopropanol, stained with Oil Red O solution at room temperature. To induce chondrogenic differentiation, cell-laden hydrogel constructs were incubated in chondrogenic differentiation medium (Procell, PD-009) and stained with Safranine O after 21 days.

2.9. Real-time polymerase chain reaction (qRT-PCR)

Total RNA from hydrogel constructs were extracted using Trizol reagent (Beyotime) according to the manufacturer's instructions. The concentrations of the extracted total RNA were determined using Nanodrop 2000 spectrophotometer (ThermoFisher, USA). Complementary DNA (cDNA) was synthesized from the extracted RNA using All-In-One 5 × MasterMix Kit (ABM, China). The obtained cDNA was used for qRT-PCR, which was performed in triplicates by using the BlasTaqTM 2 × qPCR MasterMix (ABM, China). The primers used in the qRT-PCR were listed in Table 1. The housekeeping gene, 18S, was used for data normalization. The experiment was performed in triplicates.

Table 1
Primer sequences used for real-time PCR experiments.

Name	Forward 5'-3'	Reverse 5'-3'
OCT4	GACAACCATCTGCCGCTTC	TCCTCCACCCACTTCTCCA
SOX2	GTCAGCGCCCTGCAGTACAA	GCGAGTAGGACATGCTGTAGGTG
Nanog	ACGCTGCTCCGCTCCATAAC	CAAATTCGCCTCCAAATCACTG
RUNX2	AGTTTGTTCTCTGACCGCCTC	CTGCCTGGCTCTTCTTACTGAG
BMP-2	AAGCCAAACACAAACAGCGG	TCCCCATGGCAGTAAAAGGC
OPN	AGTTTGGCAGCTCAGAGGAG	GCTTCTGAGATGGGTCAGGC
Col1a1	GCGAAGGCAACAGTCGATTC	ACTGTCTTGCCCCAAGTTCC
Col-2	GTACCTTGAGACAGCATGACG	TGAGCAAGGCCTTCTTGAGG
SOX9	AACCTTCCGCACTACAACCC	TGTGTAGACGGGTTGTTCCC
Col-1	GCGAAGGCAACAGTCGATTC	ACTGTCTTGCCCCAAGTTCC
Col-X	ATGGCTTCACAAAGAGCGGA	AGGAGTAGAGGCCGTTCGAT
FABP4	ACCAGGAAAGTGGCCGGTAT	GTACTCTCTGACCGGATGACG
C/EBPα	TAAAGCCAAACAGCGCAACG	GTGTCCAGTTCACGGCTCAG
SREBP-1c	GTAGCGTCTGCACGCCCTA	CTTGGTTGTTGATGAGCTGGAG
FAS	GGCTCAGCATGGTCGCTT	CTCCCGCCCAGCTGTCATT
18S	CATTCGAACGTCTGCCCTAT	GTTTCTCAGGCTCCCTCTCC

2.10. Transcription sequencing

The transcription sequencing was conducted by Wuhan Metware Biotechnology. Genes with log2|fold change| ≥1 considered statistically significant. Based on the Gene Ontology (GO) database (http://geneontology.org), a GO enrichment analysis was carried out. Gene set enrichment analysis (GSEA) was performed using GSEA software (http://www.broadinstitute.org/gsea) and log2 ratio of classes as metric for ranking genes. Fisher's exact test was used for GO pathway analysis.

2.11. Neovascularization in vitro and in vivo

To evaluate the effect of the CCB hydrogel on vascularization, HUVECs at a density of 2×10^4 cells/well were cultured in a conditioned medium of DPSCs-loaded CCB hydrogel and seeded onto a plate pre-coated with Matrigel (BD Biosciences, San Jose, CA, USA). The conditioned medium from the CCB and standard hydrogel was collected after 7 days of incubation. For the tube formation assay, the treated HUVECs were imaged and fixed after 6 h. The total number of branches, junctions, nodes and total vessel length were measured based on three images randomly selected for each sample using Image J software.

Wound healing assay was employed to assess the migration of the HUVECs. HUVECs were seeded in 48 well plates at a density of 3×10^4 cells/well, and incubated for 24 h to form uniform monolayer. The monolayer was then "scratched" using a pipette tip to create a linear gap through the middle of each well. Different conditioned mediums were added to study the migration of the HUVECs. Images of the wells were taken using an inverted microscope (Olympus) after 0 h and 12 h of incubation.

For *in vivo* vascular reconstruction evaluation, the hydrogels were fabricated and implanted sub-dermally on the back of nude mice. After 14 days of implantation, the samples were retrieved, embedded, and sectioned for immunohistochemical and H&E staining.

2.12. Pulpo-dentinal complex-like tissue reconstruction

Rat treated dentin matrix (TDM) was performed according to a previously published method [23]. Briefly, the first mandibular molars of SD rats were harvested. Rat dentin matrix was sliced to a length of 0.5 cm, then immersed in deionized water with an ultrasonic cleaner. Rat TDM were treated with 17 % Ethylene Diamine Tetra-acetic Acid (EDTA), 10 % EDTA, 5 % EDTA. Rat TDM were stored in sterile PBS with 100 units/mL penicillin and 100 μg/mL streptomycin, then washed in deionized water in an ultrasonic cleaner. For subcutaneous implantation, the TDMs were filled with bioprinted CCB hydrogels (CCB group) or standard hydrogels (standard group). After two months of implantation, all samples were harvested and fixed with 4 % paraformaldehyde.

2.13. Statistical analysis

Statistical analysis was performed with Excel and GraphPad Prism. Data of all measurements including *in vitro* and *in vivo* presented as mean ± standard deviation (SD). $P < 0.05$ was considered statistical significance.

3. Results

3.1. Anisotropic bioink preparation and characterization

To enable the in-situ formation of stem cell spheroids following the bioprinting process, we developed an anisotropic bioink known as cell-concentrated bioink (CCB). This bioink was formulated with dextran acting as a cell decoy to capture the encapsulated cells, and gelatin methacryloyl (GelMA) serving as the matrix to provide structural integrity. Upon the formation of the hydrogel construct, all the mixed cells were observed to be concentrated within the dextran solution, with no detectable signal in the GelMA solution (Fig. 1b). This observation suggests a more robust binding affinity between the mixed cells and the dextran polymers. The majority of the incorporated dextran could be effectively removed by either immersing the construct in phosphate-buffered saline (PBS) or by incubating it in culture media, leaving pores for cells to reside in. Concurrently, we conducted a study to examine the influence of the mixing process on the distribution of cells within the hydrogel matrix. Upon initial mixing with the GelMA polymer solution, we observed that the encapsulated cells were tightly covered with a thin layer of GelMA hydrogel (Fig. S1). This interaction could be a contributing factor to the absence of stem cell spheroid formation observed in our earlier studies [22]. This insight is crucial for refining our bioink formulation and bioprinting protocols to better control cell behavior and promote the formation of desired tissue constructs. We then investigated the parameters governing the sizes of the dextran droplets within GelMA continuous phase. The generation of this anisotropic bioink is attributed to the thermodynamic incompatibility between GelMA and dextran. The factors, including molecular weight, concentration, and volume faction, that affect thermodynamic equilibrium can govern the sizes of the dextran droplets within this system. In this work, the GelMA concentration and dextran volume fraction were investigated due to easy manipulation. The dextran microdroplets with different size distribution could be obtained using a simple combination of two phases (Fig. 1c and Fig. S2). Elevating the concentration of GelMA intensifies both the interfacial tension and viscosity, which in turn induces phase separation and results in the formation of larger dextran droplets. Additionally, the molecular weight of dextran significantly influences the size distribution of the microdroplets. According to previous study, an increase in molecular weight resulted in the formation of larger microdroplets and a wider size distribution [24]. This weight gain contributes to a rise in entropy, which in turn facilitates the aggregation propensity of the dextran phase and promotes instability.

Following the curing of the CCB hydrogel, we discovered that more than 80 % of the incorporated dextran could be effectively eliminated within a 24-h period (Fig. 1d). In addition, we also assessed the mechanical properties of the resulting hydrogel constructs (Fig. 1e). Compared to the standard GelMA hydrogel, it was softer after adding dextran. The compression strain and stress of the hydrogel decreased when the GelMA concentration decreased from 15 % to 7.5 %. The swelling ratio was characterized to assess the effect of dextran on hydrogel network formation. The dextran addition did not have a significant effect on hydrogel network formation (Fig. S3). As depicted in Fig. S4, the formed porous structure could increase the degradation speed in collagenase solution. Concurrently, it was observed that the degradation rate was enhanced by reducing the concentration of GelMA. In addition, we also measured the degradation of the hydrogels by subcutaneous implantation in a mice model (Fig. S5). Our observations revealed that a greater number of cells successfully penetrated the implanted porous hydrogel, with substantial degradation of the hydrogels evident by day 28. In contrast, no significant degradation was detected in the standard group. Following 28 days of implantation, the cells that had invaded spread throughout the hydrogels in the CCB group, whereas only a sparse number of cells were observed at the periphery in the standard group. These findings suggest that the CCB hydrogels demonstrated enhanced integration with host tissues and a more rapid degradation rate compared to the standard group.

Informed by these findings, next, we assessed the cytocompatibility of our bioink. The results of CCK-8 assay indicated that porous structure fostered the proliferation of encapsulated NIH/3T3 cells (Fig. 1f). Interestingly, our findings indicated that an elevated GelMA concentration did not impede cell proliferation. In contrast, the proliferation ratio of the encapsulated cells within the hydrogel constructs increased with GelMA concentration in experimental groups, which was contrary to previous studies [25]. Live/dead fluorescent staining revealed that our bioink had no toxicity on the encapsulated cells after 5 days of

incubation (Fig. 1g and Fig. S6). With a prolonged incubation, the addition of dextran induced the aggregation of encapsulated cells, while the cells encapsulated in standard group distributed uniformly. Scanning electron microscopy (SEM) confirmed that the cells in the 15 % group exhibited an aggregated and spreading morphology, whereas the cells in the groups of Standard, 10 % and 7.5 % maintained a rounded morphology (Fig. 1h). We further studied the effect of different formulations of the bioink on bone mesenchymal stem cells (BMSCs). Our results showed that the proliferation of BMSCs encapsulated within the bioink was enhanced by the incorporation of dextran into GelMA. However, the decreased matrix concentration did not increase the trend as we expected (Fig. S7), which was consistent with the finding in NIH/3T3 cells. The live/dead assays and SEM images also revealed the desired cell viability in the group of 15 % (Fig. 1i and Fig. S8). It is noteworthy that the encapsulated BMSCs within the 15 % hydrogel constructs exhibited a pronounced tendency towards aggregation. In summary, our proposed strategy demonstrated that this anisotropic bioink could be a potential platform to capture the mixed cells for promoting cell aggregation and enhancing cell-cell interaction. Based on the abovementioned results, 10 % (w/v) of dextran solution was mixed with 15 % (w/v) of GelMA solution at a volume ratio of 1:2 for printing tissue constructs unless otherwise indicated.

3.2. Printability of the bioink via DLP-based printing

By utilizing the optimized ink formulation, we printed several representative structures from simple 2D patterns to 3D constructs featuring complex internal and external architectures for printability evaluation. Firstly, we evaluated the stability of ink in fabricating hydrogel constructs. A 1-cm tall cylinder-shaped hydrogel was printed, and Eosin staining was applied to various sections-namely the top, middle, and bottom-to scrutinize the microstructure. Fig. S9 displayed that porous structure distributed uniformly throughout the hydrogels, demonstrating the homogeneity of ink during bioprinting process. Taking advantages of the ink, scaffolds with different shapes (e.g., wheel, heart, and meniscus) were successfully created (without cells, Fig. 2a–c). Meanwhile, we explored the cell-laden bioink's potential for printing biomimetic constructs, with cells being accurately deposited into designated areas to introduce more physiologically accurate features. Fig. 2d–f displayed that the DLP-based bioprinting using our proposed bioink would be capable of fabricating complex tissue constructs, including glioblastoma model, layered skin model, and prevascularized hepatic hydrogel model. Live/dead fluorescent images also revealed high cell viability after bioprinting (Fig. S10). In conclusion, these results demonstrated the capability of our bioink in high-precision constructs fabrication.
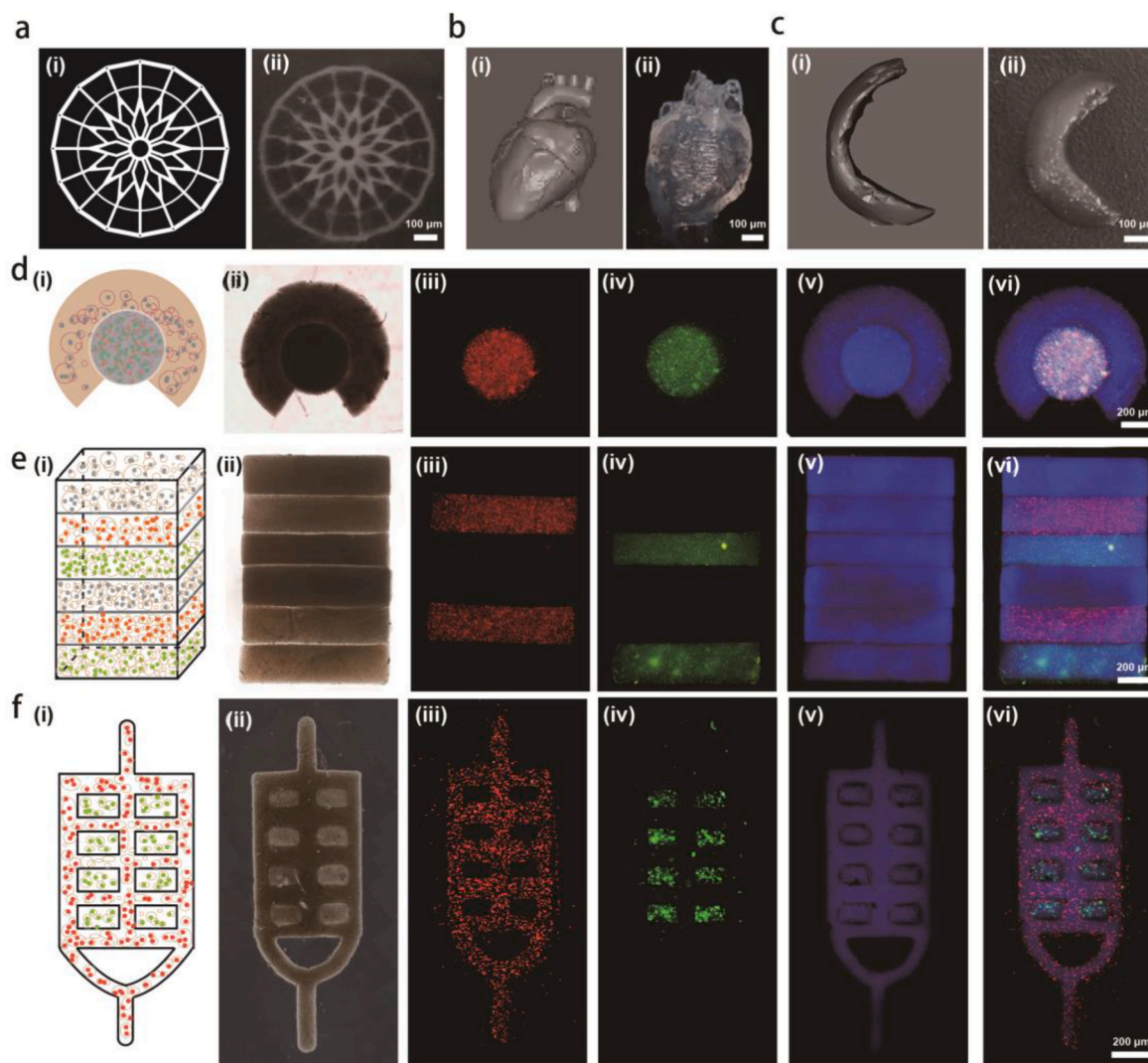

Fig. 2. Printability of the bioink using DLP-based bioprinter. (a–c) 3D-printed wheel-shaped, heart-shaped and meniscus structure. (d–f) 3D bioprinting of hydrogels with different tissue models, including glioblastoma, layered skin and prevascularized hepatic hydrogel models, respectively.

3.3. In-situ birth of stem cell spheroids within hydrogel construct

Although 3D bioprinting of multicellular spheroid-loaded hydrogels has shown great promise in tissue engineering and *in vitro* disease modeling, very limited work has been carried out to optimize the bioink for DLP-based bioprinting. In this work, we developed a cell-concentrated bioink and hypothesize that the proposed bioink could facilitate in-situ birth of stem cell spheroids. Rat dental pulp stem cells (rDPSCs) was employed for the demonstration of our hypothesis. As shown in Fig. 3a, the rDPSCs encapsulated in hydrogel displayed high cytocompatibility within 5 days of incubation. Of interest, the encapsulated MSCs aggregated in our porous hydrogels over prolonged periods, while remaining monodispersed in the standard GelMA hydrogel.

H&E and phalloidin staining (Fig. 3b and c) further confirmed that our strategy promoted the 3D clonal expansion of MSCs. In comparison, as a prevalent technique for the bioprinting of porous hydrogel constructs, our investigation revealed that a poly (ethylene oxide) (PEO)-based emulsion bioink, despite offering a uniform initial cell distribution, was incapable of promoting the aggregation of encapsulated BSMCs (Figs. S11 and S12). These findings underscore the enhanced effectiveness of our strategy in not only concentrating the suspended cells but also in encouraging their aggregation during the incubation phase. In addition to stem cell aggregation, the proliferation of encapsulated rDPSCs was significantly enhanced in the CCB group relative to the standard group (Fig. 3d). We next investigated the pluripotency of encapsulated rDPSCs in hydrogels by octamer-binding transcription
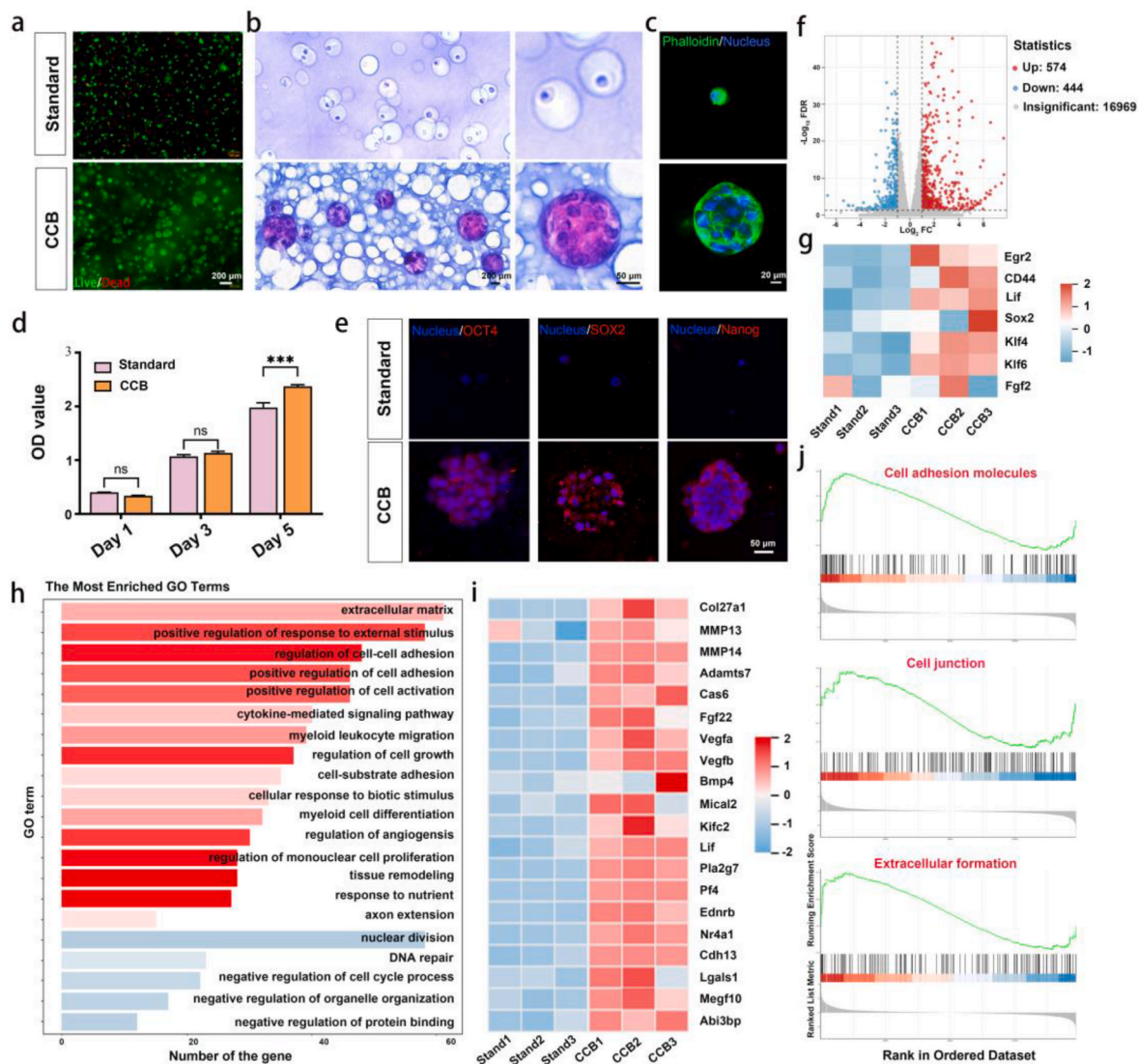

Fig. 3. 3D bioprinting of hydrogel constructs modulated the activity of encapsulated stem cells and facilitated the formation of MSCs spheroids in-situ. (a) Fluorescence micrographs showing the viability of encapsulated rDPSCs at day 5. Live cells were stained in green, while dead cells were stained in red. (b) Representative images of H&E staining of the rDPSC spheroids in hydrogels. (c) Cytoskeletal spreading in rDPSCs within hydrogel at day 5. (d) Quantitative cell proliferation results at day 1, 3, and 5 (mean $\pm$ SD, n = 3, two-way ANOVA). (e) Immunofluorescence staining of Nanog, Oct4 and Sox2 in rDPSC spheroids. Nuclei were stained with DAPI (blue). (f) Volcano plot of differentially expressed genes between these two hydrogel groups after 5 days of incubation. The red points represent the upregulated genes in CCB group. The blue points represent the down-regulated genes in CCB group. (g) Heatmaps of differentially expressed genes associated with stemness between two hydrogel groups. (h) Gene ontology (GO) enrichment analyses of upregulated and down regulated differentially expressed genes for total biological processes. (i) Heatmaps of differentially expressed genes associated with adhesion, extracellular matrix organization and angiogenesis. (j) Gene set enrichment analysis (GSEA) plot showing enrichment of the "Cell adhesion molecules", "Cell junction", and "Extracellular formation" gene set in these two hydrogel groups. The top portion of the plot shows the enrichment score (green line). The middle portion of the plot shows the appearances of the targeted genes in this gene set. The bottom portion of the plot shows the values of the ranking metric moving down the list of the ranked genes. Ns was determined as $P > 0.05$ with no statistical difference, ***$P < 0.001$.

factor 4 (OCT4), nanog homebox (NANOG) and sex determining region Y-box transcription factor 2 (SOX2) in both protein and gene expression level. The results displayed in Fig. 4e and Fig. S13 demonstrated that the expression of stemness markers (OCT4, SOX2, and NANOG) were significantly upregulated in CCB group. This result demonstrated the distinct advantage of our proposed approach in encapsulating stem cells and fostering the formation of spheroids, which in turn enhanced the maintenance of their stemness.

To further investigate the transcriptional response, transcriptome sequencing analysis (RNA-seq) of rDPSCs cultured in different hydrogel constructs was detected to analyze their differences. The volcano plot identified that 1018 genes differentially expressed between the two groups, with 444 genes downregulated and 574 genes upregulated (Fig. 3f). The expression of its stemness-related genes (e.g., Egr2, CD44, Lif, Klf4, and Klf6) was significantly up-regulated in CCB group (Fig. 3g). Gene ontology (GO) enrichment of biological process showed the enrichment of extracellular matrix, response to external stimulus, regulation of cell-cell adhesion, cytokine-mediated signaling pathway, response to nutrient, and tissue remodeling (Fig. 3h). In addition, GO enrichment of molecular function indicated the enrichment of angiogenesis, including the response of angiogenesis, and sprouting angiogenesis. A variety of studies have confirmed the formation of stem cell spheroids can increase the angiogenesis properties comparing to 2D cell culture [26]. In order to further investigate the transcriptional response of in situ rDPSC spheroids formation within CCB hydrogel constructs, we generated a heatmap to display the expression change of representative genes associated with adhesion, extracellular matrix organization and angiogenesis (Fig. 3i). Our analysis identified Cdh13, Lgals1, Megf10 and Abi3bp were tightly correlated with cell adhesion, and Col27a1, Mmp13, Mmp14, Adamts7, and Gas6 as crucial genes involved in the regulation of extracellular matrix organization, while Fgf22, Vegfa, Vegfb and Bmp4 were involved in angiogenesis. Consistently, gene set enrichment analysis (GSEA) indicated the enrichment of positive regulation of cell adhesion molecular, cell junction, and extracellular formation (Fig. 3j). Collectively, the encapsulation of rDPSC by CCB hydrogel promoted the enrichment of these biological processes and molecular functions, which are conducive to tissue regeneration.

To investigate the differentiation capabilities of encapsulated rDPSCs, the prepared hydrogel constructs were incubated with the corresponding differentiation medium. As shown in Fig. 4a–d, the rDPSCs in the CCB group expressed higher osteogenic marker genes over the culture period than those cells in the standard group. At day 21, the level of BMP-2 expression was about 15-fold up-regulated in the CCB group, compared with that of standard. Col-1, OPN, and RUNX2 expression were also increased in the CCB group at all time points. The mineral deposits were then stained with 1 % alizarin red S (a functional osteoblast marker) to assess calcium deposits. The images displayed in Fig. 4m and Fig. S14a suggested that employment of our advanced strategy resulted in more mineral deposits of encapsulated rDPSCs within CCB group. Similarly, the rDPSCs encapsulated in our experimental group displayed higher chondrogenic gene expression level for type II collagen and SOX9, compared to that of standard group (Fig. 4e and f). To further determine the capability of encapsulated cells in chondrogenic differentiation without hypertrophy, we also assessed the expression of hypertrophic marker genes (Col-1 and Col-x). Conversely, while gene expression for Col-1 and Col-x decreased over the culture period in standard group, their expression in encapsulated rDPSCs was still much higher than that of in the CCB group (Fig. 4g and h). After 21 days of induction, safranin O staining was employed to identify the presence of proteoglycan-rich matrix. A vigorous intensity of safranin O staining presented in the CCB group, indicating the greatest degree of GAG production (Fig. 4n and Fig. S14b). The adipogenic differentiation of encapsulated rDPSCs in hydrogel constructs also displayed similar results to that of osteogenic and chondrogenic differentiation (Fig. 4i–l,
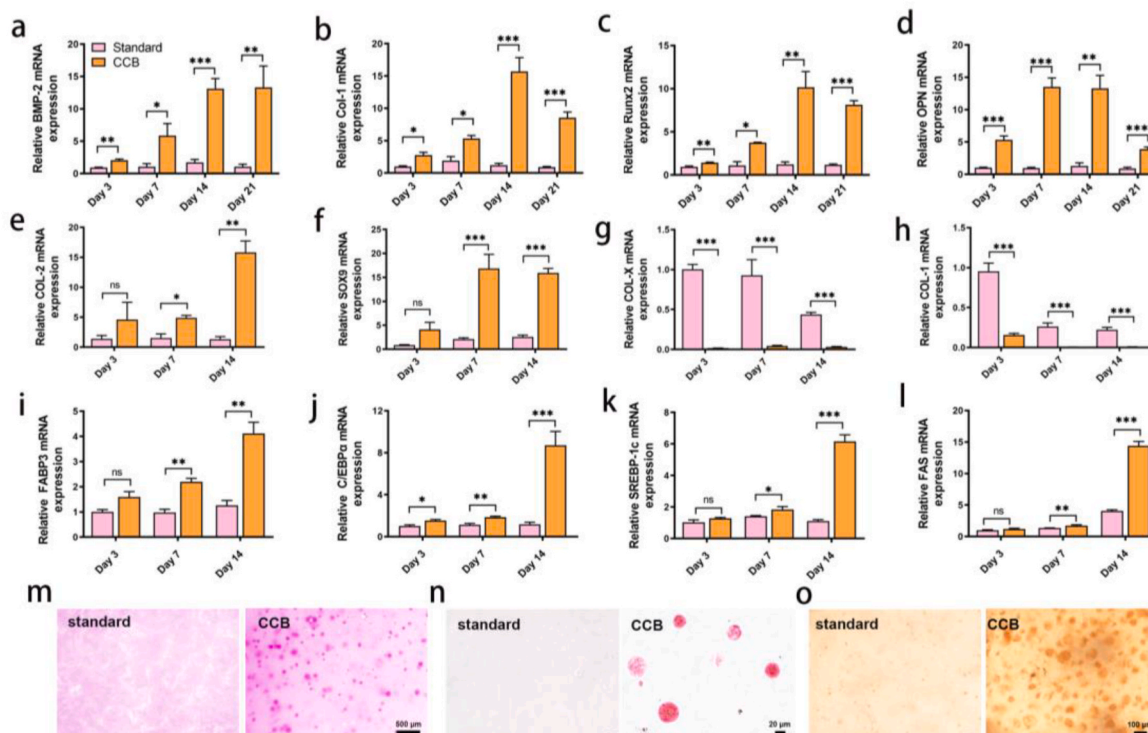
Fig. 4. Multilineage differentiation of rDPSCs in hydrogel. (a–d) Quantification of gene expression of BMP2, Col-1, RUNX2, and OPN (mean ± SD, n = 3, two-way ANOVA). (e–h) Expression levels of cartilage-specific genes, including Col-2, SOX9, Col-x, and Col-1 (mean ± SD, n = 3, two-way ANOVA). (i–l) Expression levels of adipogenic-specific genes, including FABP3, c/EBPα, SREBP-1c and FAS (mean ± SD, n = 3, two-way ANOVA). (m) Optical microscope images of Alizarin Red S staining. (n) Safranin O-staining of the rDPSCs encapsulated in hydrogels. (o) Oil Red O staining of the rDPSCs encapsulated in hydrogels. Ns was determined as $P > 0.05$ with no statistical difference, $*P < 0.05$, $**P < 0.01$, $***P < 0.001$.

Fig. 4o, and Figure S14c). Altogether, these results indicated that CCB hydrogel can promote the in-situ birth of stem cell spheroids to enhance the proliferation, pluripotency, and differentiation.

3.4. Neovascularization improved by stem cell spheroids hydrogel constructs

Owing to the spherical structure and biological microenvironment, MSC spheroids were demonstrated to enhance the secretion of angiogenic and anti-apoptotic factors [27]. Specifically, MSCs within spheroids have been found to markedly increase the expression of key angiogenic growth factors, including hepatocyte growth factor (HGF), vascular endothelial growth factor (VEGF), and fibroblast growth factor 2 (FGF2), when compared to their counterparts in two-dimensional cell monolayers [28]. In this study, human umbilical vein endothelial cells (HUVECs) were utilized to assess the angiogenic potential of the CCB hydrogel constructs through tube formation and migration assays. As

shown in Fig. 5a, HUVECs cultured in the conditioned medium derived from DPSC-loaded CCB hydrogel constructs exhibited a pronounced ability to form capillary-like network structures, surpassing those observed in the control group. Furthermore, upon a detailed examination of quantitative metrics—encompassing the number of junctions, branches, nodes, and tube length—it was clear that the CCB group exhibited substantially higher values in comparison to the standard group. This marked improvement in angiogenic parameters underscored the enhanced performance of the CCB hydrogel constructs in facilitating the formation of vascular networks (Fig. 5b). Additionally, the CCB group demonstrated a notably higher count of migrated HUVECs compared to the standard group, as evidenced in Fig. 5c. This substantial increase in cell migration within the CCB group highlights the superior ability of the CCB hydrogel constructs to promote endothelial cell motility, which is a critical aspect of angiogenesis.

Next, we prepared the hybrid cell spheroids by combining hDPSCs and HUVECs and evaluated the neovascularization *in vivo*. The
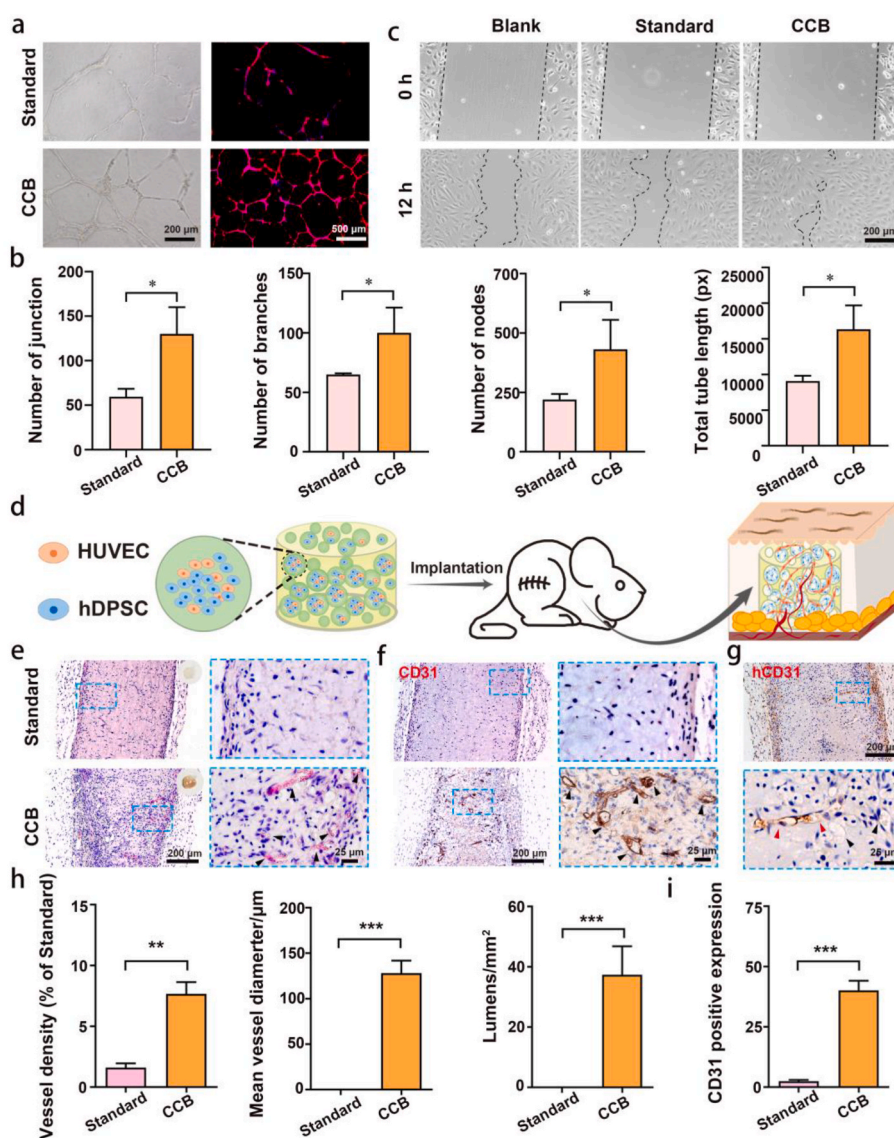

Fig. 5. Application of bioprinted hydrogels in neovascularization. (a) Bright-field (left) and immunofluorescent (right) images of HUVECs in different conditioned mediums. (b) Corresponding qualitative analysis of vascular network organization indexes, including branches, junctions, nodes, and total length. (c) Wound-healing assays of the treated HUVECs with different conditioned mediums. (d) Schematic diagram of vascular regeneration *in vivo*. (e) Representative H&E images of angiogenesis *in vivo*. (f) Immunostaining images for CD31 at 14 days post-implantation. (g) Immunostaining images for hCD31 at 14 days post-implantation in CCB group. (h) Quantification of the vessel density, mean vessel diameter and lumens density from (e) (mean ± SD, n = 3, two-way ANOVA). (i) Quantification analysis of CD31 expression in (f) (mean ± SD, n = 3, two-way ANOVA). **$P < 0.01$, ***$P < 0.001$.

bioprinted hydrogel was implanted sub-dermally on the back of nude mice (Fig. 5d). After two weeks, the implanted hydrogel constructs were harvested for histological evaluation. As shown in Fig. 5e, a rich network of blood vessels filled with erythrocytes was observed throughout the hydrogels in the CCB group, indicating a robust vascularization. In stark contrast, the standard GelMA hydrogel exhibited an almost negligible presence of such vascular structures. We quantified the vessel density, mean vessel diameter, and lumen density according to the H&E images. All these parameters were highly upregulated in the CCB group than those in the standard group (Fig. 5h). In our further exploration of the microvascular structures, we conducted an immunohistochemistry analysis by staining the tissue sections with a CD31 antibody (a marker for endothelial cells). The findings (Fig. 5f and i) revealed a significantly higher presence of CD31-positive area within the CCB group, suggesting that our hydrogel constructs effectively facilitated the *in vivo* formation of new blood vessels. Moreover, the microvessels exhibited positive staining for human CD31, which confirmed that the vascular lumens were lined with the implanted HUVECs (Fig. 5g). A meticulous examination of these human microvessels revealed the presence of murine erythrocytes, signifying that functional connections, or anastomoses, had been established with the surrounding murine vasculature. This

critical observation indicated that the microvascular network within the CCB hydrogel constructs was indeed generated by the implanted cells, rather than merely being a result of host blood vessel infiltration.

3.5. Pulpo-dentinal complex-like tissue reconstruction

Infection to dental pulp, causing 400, 000 new cases annually in the USA, commonly needs surgical removal of the diseased pulp or even the tooth [29]. Root canal treatment (RCT) remains the standard clinical treatment to preserve the diseased teeth and realize their partial functions, while the treated tooth commonly becomes brittle and fractured, showing a high risk of re-infections and still losing the choice of retaining tooth [30]. Innovative approaches are being explored to enhance the outcomes of endodontic treatments. Qian et al. combined microgels and DLP-based bioprinting technology to prepare hDPSC-loaded microspheres and found the formation of vascular, neural, and odontogenetic tissues in heterotopic implantation tests [31], suggesting the application potential of DLP-based bioprinting in endodontic regeneration. In this study, a proof-of-concept of study was further performed to prepare hydrogels encapsulating rDPSCs for the potential of supporting the regenerative dentin and neovascular-like
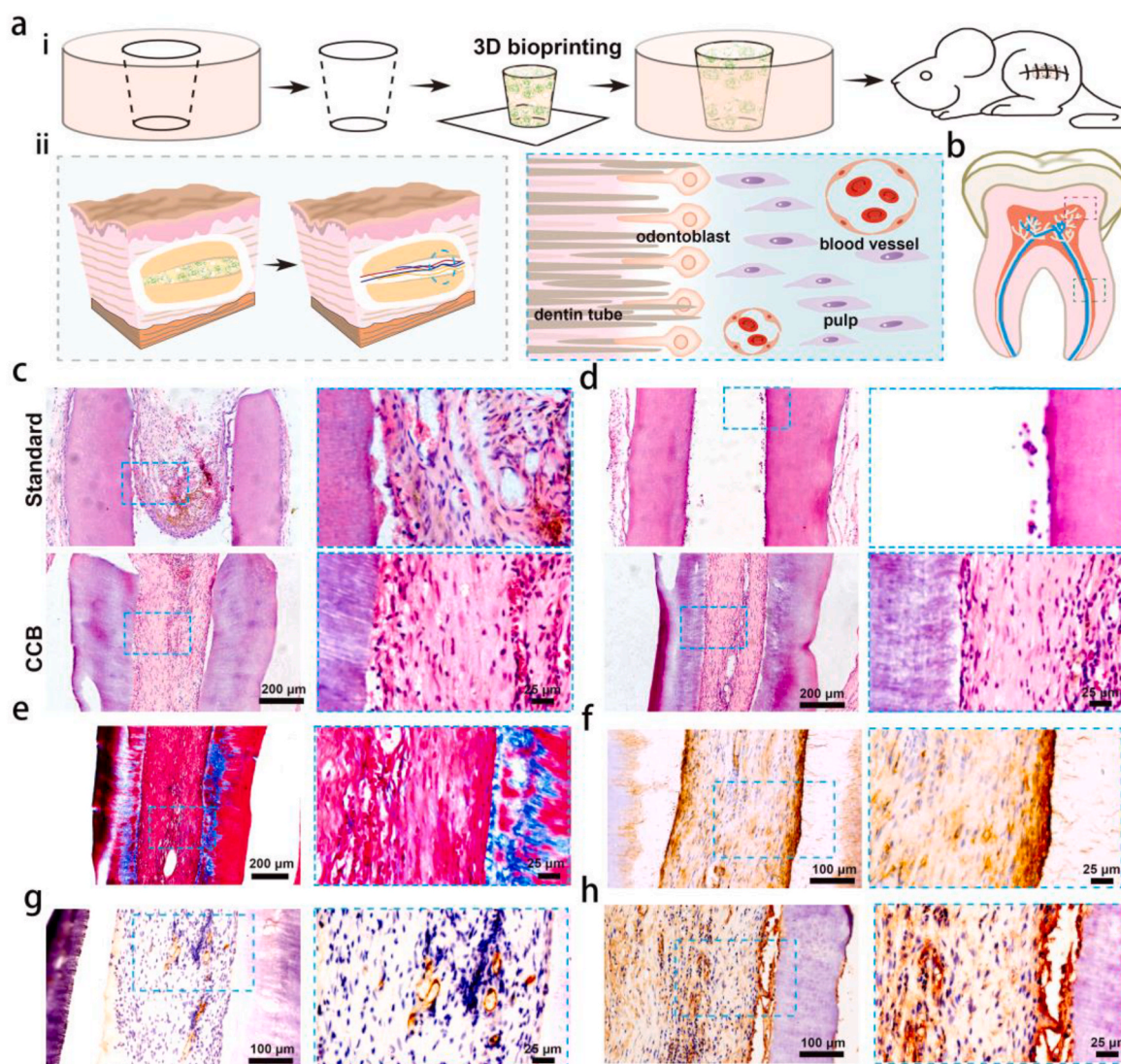
Fig. 6. Reconstitution of dental pulpo-like tissue in a subcutaneous model. (a) Schematic diagram showing the i) fabrication of hydrogel constructs with TDM and ii) their application in regenerative endodontic treatment. (b) Schematic diagram of pulp regeneration sampling, with red boxes indicating border and green boxes indicating the center. (c and d) H&E staining of regenerated pulpo dentin tissue at different sites. (e) Masson's Trichrome staining of regenerated pulpo dentin tissue in CCB group. Immunohistological staining of (f) dentin marker (DSPP), (g) blood vessel marker (CD31), and (h) nerve tissue marker (NF200) in CCB group.

structures. Rat-derived treated dentin matrix (TDM) root slices were filled with 3D-bioprinted hydrogels and implanted into subcutaneous SD rats (Fig. 6a–i), with the aim of pursuing angiogenesis and odontogenic differentiation (Fig. 6a–ii). It is noteworthy that TDM, whether sourced from rats or humans, has the capacity to express key proteins such as nestin, collagen type I (COL-I), and cementum attachment protein (CAP). The latter, CAP, is particularly significant due to its role in guiding dental stem cells toward differentiation into dentin [32]. Therefore, they are commonly used as heterotopic models to evaluate endodontic regeneration. After 8 weeks of implantation, histological evaluations were conducted at both the central and peripheral regions of the implantation sites (Fig. 6b). H&E staining results (Fig. 6c and d) revealed that the scaffold in the standard group was devoid of cellular content, and there was minimal tissue infiltration at the proximal site. In the CCB group, histological evaluations revealed significant advancements in tissue regeneration. The TDM scaffolds were observed to be filled with newly formed tissues, including the emergence of blood vessels and the development of dentin-like structures. Also, collagen fibers were clearly observed in the CCB group by Masson' trichrome staining (Fig. 6e). Immunohistochemistry experiments showed an increased expression of odontogenetic (DSPP, Fig. 6f and Fig. S15a), vascular (CD31, Fig. 6g and Fig. S15b), neural (NF200, Fig. 6h) markers in the CCB group, confirming the effective pulpo-dentinal complex-like tissue reconstruction using CCB hydrogels.

4. Discussion

DLP-based bioprinting technology, which employs a digital micromirror device to manipulate patterned light, stands as a leading additive manufacturing technique for the creation of hydrogel constructs with tissue-mimicking shape and functions [33]. After tissue constructs accomplishment, the construct matrix affects the encapsulated cells by surrounding biochemical/biophysical cues (e.g., geometric structure, viscosity, and adhesion), while the encapsulated cells can regulate the matrix by paracrine and cell force *in vitro* and *in vivo* [34]. The bioink is a paramount component in the fabrication process, as it determines the cytocompatibility and mechanical tunability of the hydrogel constructs. Despite its importance, the optimization of bioink to meet these specific requirements has been a relatively understated area of research. To achieve high-performance DLP-based bioprinting, in this study, a facile and practical strategy was proposed to prepare hydrogel constructs with abilities of inducing in-situ birth of stem cell spheroids. The optimized bioink could anchor and concentrate the mixed cells in the dextran phase throughout the printing process. Although the addition of dextran induced the phase separation in bioink, the hydrogel constructs could be printed without losing structural complexity and fidelity. After printing, the dextran was removed to formulate a porous structure, triggering the spheroids of the encapsulated stem cells. In vitro assessments validated that these printed hydrogel constructs were not only capable of preserving but also enhancing the stemness of the embedded stem cells, which is a significant advancement for applications in tissue engineering and regenerative medicine. Furthermore, *in vivo* analyses focusing on the neovascularization and the regeneration of pulpo-dentinal complex-like tissues demonstrated that hydrogel constructs featuring in-situ spheroid formation significantly outperformed traditional bioprinted hydrogel constructs in terms of tissue regenerative capabilities.

The modulation of cell-cell and cell-matrix interactions is crucial for the efficacy of printed hydrogel constructs, as these interactions significantly influence cell behavior and function [35]. By fine-tuning the geometry of cell adhesion, it is possible to regulate these interactions, thereby precisely controlling cellular activities [36]. GelMA, as a photocrosslinkable derivate of gelatin has been widely used as a base component in formulating bioink for its biocompatibility, tunable mechanical property, and cost-effectiveness [37,38]. With the development of tissue engineering and biomaterial science, GelMA-based bioink has been extensively employed as the scaffolds to support cell loading and

tissue regeneration [39–41]. However, the dense structure of traditional GelMA hydrogels can sometimes restrict cell-cell and cell-matrix interactions, leading to less desirable outcomes.

To overcome the aforementioned limitations, several innovative strategies were proposed to develop novel GelMA-based bioinks with adjustable mechanical properties that also provide a conducive environment for cell support [42,43]. On one hand, the cell laden microgels were utilized as bioink to enhance the interaction of the cell-cell and cell-matrix, where the microgels, as the sacrificed phase, would be removed after bioprinting [44]. While it was commonly used in nozzle-based bioprinting technology. On the other hand, porous GelMA hydrogels prepared by freeze-drying or aqueous emulsions can promote cell adhesion, migration, and spreading [45,46]. In turn, the reorganized cytoskeleton causes the deformation of ECM and activates mechanical signaling pathways, such as YAP/TAZ signal pathway [47]. In our previous studies, we demonstrated the feasibility of porous hydrogel constructs via GelMA/Dextran emulsion bioink in overcoming the shortages of cell post-loading methods [48]. Nevertheless, the bioinks were commonly prepared by directly mixing the harvested cells and emulsion, which resulted in the randomly distribution of mixed cells. The cells in the dense GelMA network still had a round morphology and less cell viability. In this work, we found that pre-loading the cells with dextran could function as a decoy to absorb the mixed cells and direct them away from GelMA phase. This feature showed advantageous abilities to concentrate the mixed cells in bioink and favor cell-cell interactions during incubation. Meanwhile, the higher surface area was demonstrated to control the focal adhesion and mechanotransduction process [49]. In addition, the formed pores facilitated the diffusion and exchange of oxygen and nutriment to enable a favorable microenvironment.

Stemness maintenance, referred to the renewal and differentiation capabilities of stem cells, is a pivotal aspect of cell therapy and regenerative medicine that requires meticulous optimization [50,51]. Previous research has demonstrated that the intricate interplay between intrinsic cellular properties and extrinsic environmental factors could significantly shape the vital attribute of stemness. Various strategies have been employed to modulate this characteristic, including the supplementation of growth factors, the application of gene transduction techniques, and the physicochemical modification of biomaterials to create an optimal niche for stem cell maintenance and differentiation [52–54]. Nevertheless, these traditional methods have some shortcomings that need to be concerned, particularly in hydrogel constructs. For instance, the application of growth factors (e.g., bFGF, TGF-beta, and interleukin) to facilitate the stemness of cultured stem cells is delicately balanced; they must be administered in a dose-dependent manner to avoid a decline in cell proliferation once a certain threshold is surpassed [55,56]. Besides, the safety should be considered and growth factors/cytokines might change the genetic response and protein expression. In this work, we explored a simple and practical design of bioink to enable a high cell density. In the dextran region, the harvested cells with a high cell density enhanced the cell-cell interactions and facilitated the aggregation and spheroids of the encapsulated stem cells. Anupam A. K. Das et al. also found that the cell in dextran phase of an aqueous emulsion rendered spheroid generation [57]. Although the dextran will be removed from the hydrogel constructs in our study, this process will last for several days and the remaining dextran within constructs can also function. The presence of pluripotency markers, including OCT-4, SOX-2, and Nanog, is of importance for the renewal and differentiation abilities of stem cells, but they were rarely observed in standard GelMA group. Notably, treating stem cells with our proposed strategy significantly enhanced expression of these markers, demonstrating the superior capabilities in maintaining stemness. Next, we chose an endodontic regeneration model for a proof-of-concept demonstration of our proposed biomaterials with broad-spectrum applicability due to pulpo-dentinal complex tissues with several types of basic tissues containing vessels, nerves, and stiff dentin tissues. After implantation of

DPSC-loaded CCB hydrogel constructs in a heterotopic model, histological staining suggested that the engineered constructs fostered a more robust regeneration of pulpo-dentinal complex-like tissue compared to the standard hydrogel-only constructs, which might be attributed to the synergistic effects of the porous architecture and the presence of stem cell spheroids.

In this study, we opted for GelMA-based materials to fabricate the hydrogel constructs via 3D printing; however, our system is not limited to this specific biomaterial. A spectrum of other biomaterials, such as silk fibroin, hyaluronic acid, and alginate, can be seamlessly integrated into our 3D-printing framework. Such flexibility in tuning the composition allows researchers to easily modulate the degradation and mechanical properties, resulting in tissue-matching physicochemical environment for optimal performance. On top of that, dextran polymers can also be modified with functional groups for regulating the interactions between cell-cell and cell-matrix. Meanwhile, the commercial microsphere preparation instruments [58] can be employed to fabricate microgels with a core-shell structure, in which the core is made of dextran/cells and shell is made of GelMA hydrogel, to meet different applications. These microgels might fabricate hydrogels encapsulating stem cell spheroids with a uniform size. In the future, different disease models *in vitro* and animal models *in vivo* should be studied to further verify the effectiveness of our strategy.

5. Conclusions

In the present study, we have demonstrated the suitability of a cell-concentrated bioink to support the DLP-based bioprinting of tissue constructs with stem cell spheroids formation in situ. The bioink we developed has been proven to facilitate the fabrication of high-performance hydrogel construct with significantly improved cell viability, while preserving their structural complexity and fidelity. Additionally, these constructs effectively concentrate the embedded cells within the dextran phase. The stem cells affected by curved morphology and high cell density are inclined to aggregate into spheroids, leading to amplified stemness and differentiation potential. Furthermore, our hydrogels have demonstrated the capacity to support vascularization and regenerative dentin *in vivo*. Based on these data, we propose a facile and practical strategy for in-situ birth of stem cell spheroids bioprinted hydrogel tissue constructs via using cell-concentrated bioink, showing great potential in tissue engineering and regenerative medicine.

Ethics approval and consent to participate

The animal experimental procedures were approved by the Institutional Animal Care and Use Committee (IACUC) of the Army Medical University (AMUWEC20212172).

CRediT authorship contribution statement

Shunyao Zhu: Writing – original draft, Methodology, Conceptualization, Funding acquisition, Writing – review & editing. **Xueyuan Liao:** Methodology, Investigation. **Yue Xu:** Writing – review & editing, Formal analysis. **Nazi Zhou:** Software, Investigation, Formal analysis. **Yingzi Pan:** Data curation, Formal analysis, Validation. **Jinlin Song:** Writing – review & editing. **Taijing Zheng:** Writing – review & editing. **Lin Zhang:** Writing – review & editing, Formal analysis. **Liyun Bai:** Writing – review & editing, Formal analysis. **Yu Wang:** Formal analysis, Writing – review & editing. **Xia Zhou:** Funding acquisition, Writing – original draft. **Maling Gou:** Writing – review & editing. **Jie Tao:** Writing – review & editing, Supervision, Project administration, Funding acquisition, Formal analysis, Conceptualization, Methodology. **Rui Liu:** Writing – review & editing, Project administration, Funding acquisition.

Appendix A. Supplementary data

Supplementary data to this article can be found online at https://doi.org/10.1016/j.bioactmat.2024.09.033.

References

[1] R. Levato, O. Dudaryeva, C.E. Garciamendez-Mijares, B.E. Kirkpatrick, R. Rizzo, J. Schimelman, K.S. Anseth, S. Chen, M. Zenobi-Wong, Y.S. Zhang, Light-based vat-polymerization bioprinting, Nat. Rev. Methods Prim. 3 (2023) 47, https://doi.org/10.1038/s43586-023-00231-0.

[2] B. Grigoryan, S.J. Paulsen, D.C. Corbett, D.W. Sazer, C.L. Fortin, A.J. Zaita, P. T. Greenfield, N.J. Calafat, J.P. Gounley, A.H. Ta, F. Johansson, A. Randles, J. E. Rosenkrantz, J.D. Louis-Rosenberg, P.A. Galie, K.R. Stevens, J.S. Miller, Multivascular networks and functional intravascular topologies within biocompatible hydrogels, Science 364 (2019) 458–464, https://doi.org/10.1126/science.aav9750 (80-.).

[3] J.R. Tumbleston, D. Shirvanyants, N. Ermoshkin, R. Janusziewicz, A.R. Johnson, D. Kelly, K. Chen, R. Pinschmidt, J.P. Rolland, A. Ermoshkin, E.T. Samulski, J. M. DeSimone, Continuous liquid interface production of 3D objects, Science 347 (2015) 1349–1352, https://doi.org/10.1126/science.aaa2397 (80-.).

[4] C.A. Murphy, K.S. Lim, T.B.F. Woodfield, Next evolution in organ-scale biofabrication: bioresin design for rapid high-resolution vat polymerization, Adv. Mater. 34 (2022), https://doi.org/10.1002/adma.202107759.

[5] K. Liang, C. Leong, J.M. Loh, N. Chan, L. Lim, Y.I. Lam, T.L. Dawson, H.L. Tey, A 3D-printed transepidermal microprojection array for human skin microbiome sampling, Proc. Natl. Acad. Sci. USA 119 (2022) 1–9, https://doi.org/10.1073/pnas.2203556119.

[6] X. Zhang, W. Jiang, C. Xie, X. Wu, Q. Ren, F. Wang, X. Shen, Y. Hong, H. Wu, Y. Liao, Y. Zhang, R. Liang, W. Sun, Y. Gu, T. Zhang, Y. Chen, W. Wei, S. Zhang, W. Zou, H. Ouyang, Msx1+ stem cells recruited by bioactive tissue engineering graft for bone regeneration, Nat. Commun. 13 (2022), https://doi.org/10.1038/s41467-022-32868-y.

[7] P.S. Zieliński, P.K.R. Gudeti, T. Rikmanspoel, M.K. Włodarczyk-Biegun, 3D printing of bio-instructive materials: toward directing the cell, Bioact. Mater. 19 (2023) 292–327, https://doi.org/10.1016/j.bioactmat.2022.04.008.

[8] A. Lee, A.R. Hudson, D.J. Shiwarski, J.W. Tashman, T.J. Hinton, S. Yerneni, J. M. Bliley, P.G. Campbell, A.W. Feinberg, 3D bioprinting of collagen to rebuild components of the human heart, Science 365 (2019) 482–487, https://doi.org/10.1126/science.aav9051 (80-.).

[9] N. Huebsch, E. Lippens, K. Lee, M. Mehta, S.T. Koshy, M.C. Darnell, R.M. Desai, C. M. Madl, M. Xu, X. Zhao, O. Chaudhuri, C. Verbeke, W.S. Kim, K. Alim, A. Mammoto, D.E. Ingber, G.N. Duda, D.J. Mooney, Matrix elasticity of void-forming hydrogels controls transplanted-stem-cell-mediated bone formation, Nat. Mater. 14 (2015) 1269–1277, https://doi.org/10.1038/nmat4407.

[10] S. Lee, J. Lee, S. Choi, E. Kim, H. Kwon, J. Lee, S.M. Kim, H. Shin, Biofabrication of 3D adipose tissue via assembly of composite stem cell spheroids containing adipo-inductive dual-signal delivery nanofibers, Biofabrication 16 (2024) 035018, https://doi.org/10.1088/1758-5090/ad4a67.

[11] W. Kim, Y. Gwon, S. Park, H. Kim, J. Kim, Therapeutic strategies of three-dimensional stem cell spheroids and organoids for tissue repair and regeneration, Bioact. Mater. 19 (2023) 50–74, https://doi.org/10.1016/j.bioactmat.2022.03.039.

[12] Y. Zhang, S. Ai, Z. Yu, L. Wang, H. Tao, B. Wang, D. Kong, Z. Yang, Y. Wang, Mesenchymal stem cell spheroids induced by supramolecular nanofibers for diabetic wound healing, Adv. Funct. Mater. 2314607 (2024) 1–15, https://doi.org/10.1002/adfm.202314607.

[13] N. Di Caprio, M.D. Davidson, A.C. Daly, J.A. Burdick, Injectable MSC spheroid and microgel granular composites for engineering tissue, Adv. Mater. 2312226 (2024) 1–14, https://doi.org/10.1002/adma.202312226.

[14] D. Banerjee, Y.P. Singh, P. Datta, V. Ozbolat, A. O'Donnell, M. Yeo, I.T. Ozbolat, Strategies for 3D bioprinting of spheroids: a comprehensive review, Biomaterials 291 (2022) 121881, https://doi.org/10.1016/j.biomaterials.2022.121881.

[15] A.C. Daly, M.D. Davidson, J.A. Burdick, 3D bioprinting of high cell-density heterogeneous tissue models through spheroid fusion within self-healing hydrogels, Nat. Commun. 12 (2021) 753, https://doi.org/10.1038/s41467-021-21029-2.

[16] S. Jeon, J.H. Heo, M.K. Kim, W. Jeong, H.W. Kang, High-precision 3D bio-dot printing to improve paracrine interaction between multiple types of cell spheroids, Adv. Funct. Mater. 30 (2020) 1–12, https://doi.org/10.1002/adfm.202005324.

[17] R. Levato, O. Dudaryeva, C.E. Garciamendez-Mijares, B.E. Kirkpatrick, R. Rizzo, J. Schimelman, K.S. Anseth, S. Chen, M. Zenobi-Wong, Y.S. Zhang, Light-based vat-polymerization bioprinting, Nat. Rev. Methods Prim. 3 (2023), https://doi.org/10.1038/s43586-023-00231-0.

[18] J. Zeng, X. Chen, J. Zhang, Y. Qin, K. Zhang, X. Li, H. Cui, Stem cell spheroids production for wound healing with a reversible porous hydrogel, Mater. Today Adv. 15 (2022) 100269, https://doi.org/10.1016/j.mtadv.2022.100269.

[19] K. Zhang, S. Yan, G. Li, L. Cui, J. Yin, In-situ birth of MSCs multicellular spheroids in poly(l -glutamic acid)/chitosan scaffold for hyaline-like cartilage regeneration, Biomaterials 71 (2015) 24–34, https://doi.org/10.1016/j.biomaterials.2015.08.037.

[20] X. Yang, B. Yang, Y. Deng, X. Xie, Y. Qi, G. Yan, X. Peng, P. Zhao, L. Bian, Coacervation-mediated cytocompatible formation of supramolecular hydrogels with self-evolving macropores for 3D multicellular spheroid culture, Adv. Mater. 35 (2023) 1–9, https://doi.org/10.1002/adma.202300636.

[21] J. Tao, H. Liu, W. Wu, J. Zhang, S. Liu, J. Zhang, Y. Huang, X. Xu, H. He, S. Yang, M. Gou, 3D-Printed nerve conduits with live platelets for effective peripheral nerve repair, Adv. Funct. Mater. 30 (2020) 2004272, https://doi.org/10.1002/adfm.202004272.

[22] J. Tao, S. Zhu, X. Liao, Y. Wang, N. Zhou, Z. Li, H. Wan, Y. Tang, S. Yang, T. Du, Y. Yang, J. Song, R. Liu, DLP-based bioprinting of void-forming hydrogels for enhanced stem-cell-mediated bone regeneration, Mater. Today Bio 17 (2022) 100487, https://doi.org/10.1016/j.mtbio.2022.100487.

[23] D. Wang, Y. Lyu, Y. Yang, S. Zhang, G. Chen, J. Pan, W. Tian, Schwann cell-derived EVs facilitate dental pulp regeneration through endogenous stem cell recruitment via SDF-1/CXCR4 axis, Acta Biomater. 140 (2022) 610–624, https://doi.org/10.1016/j.actbio.2021.11.039.

[24] S. Yi, Q. Liu, Z. Luo, J.J. He, H.L. Ma, W. Li, D. Wang, C. Zhou, C.E. Garciamendez, L. Hou, J. Zhang, Y.S. Zhang, Micropore-Forming gelatin methacryloyl (GelMA) Bioink Toolbox 2.0: designable tunability and adaptability for 3D bioprinting applications, Small 18 (2022) 1–14, https://doi.org/10.1002/smll.202106357.

[25] J.W. Nichol, S.T. Koshy, H. Bae, C.M. Hwang, S. Yamanlar, A. Khademhosseini, Cell-laden microengineered gelatin methacrylate hydrogels, Biomaterials 31 (2010) 5536–5544, https://doi.org/10.1016/j.biomaterials.2010.03.064.

[26] Y. Qiao, Z. Xu, Y. Yu, S. Hou, J. Geng, T. Xiao, Y. Liang, Q. Dong, Y. Mei, B. Wang, H. Qiao, J. Dai, G. Suo, Single cell derived spheres of umbilical cord mesenchymal stem cells enhance cell stemness, survival ability and therapeutic potential on liver failure, Biomaterials 227 (2020) 119573, https://doi.org/10.1016/j.biomaterials.2019.119573.

[27] M.W. Laschke, M.D. Menger, Life is 3D: boosting spheroid function for tissue engineering, Trends Biotechnol. 35 (2017) 133–144, https://doi.org/10.1016/j.tibtech.2016.08.004.

[28] S.H. Bhang, S.W. Cho, W.G. La, T.J. Lee, H.S. Yang, A.Y. Sun, S.H. Baek, J.W. Rhie, B.S. Kim, Angiogenesis in ischemic tissue produced by spheroid grafting of human adipose-derived stromal cells, Biomaterials 32 (2011) 2734–2747, https://doi.org/10.1016/j.biomaterials.2010.12.035.

[29] K. Xuan, B. Li, H. Guo, W. Sun, X. Kou, X. He, Y. Zhang, J. Sun, A. Liu, L. Liao, S. Liu, W. Liu, C. Hu, S. Shi, Y. Jin, Deciduous autologous tooth stem cells regenerate dental pulp after implantation into injured teeth, Sci. Transl. Med. 10 (2018) eaaf3227, https://doi.org/10.1126/scitranslmed.aaf3227.

[30] S. Wang, X. Xing, W. Peng, C. Huang, Y. Du, H. Yang, J. Zhou, Fabrication of an exosome-loaded thermosensitive chitin-based hydrogel for dental pulp regeneration, J. Mater. Chem. B 11 (2023) 1580–1590, https://doi.org/10.1039/d2tb02073d.

[31] Y. Qian, J. Gong, K. Lu, Y. Hong, Z. Zhu, J. Zhang, Y. Zou, F. Zhou, C. Zhang, S. Zhou, T. Gu, M. Sun, S. Wang, J. He, Y. Li, J. Lin, Y. Yuan, H. Ouyang, M. Yu, H. Wang, DLP printed hDPSC-loaded GelMA microsphere regenerates dental pulp and repairs spinal cord, Biomaterials 299 (2023) 122137, https://doi.org/10.1016/j.biomaterials.2023.122137.

[32] Y. Kobayashi, J. Nouet, E. Baljinnyam, Z. Siddiqui, D.H. Fine, D. Fraidenraich, V. A. Kumar, E. Shimizu, iPSC-derived cranial neural crest-like cells can replicate dental pulp tissue with the aid of angiogenic hydrogel, Bioact. Mater. 14 (2022) 290–301, https://doi.org/10.1016/j.bioactmat.2021.11.014.

[33] L. Yue, Y. Su, M. Li, L. Yu, X. Sun, J. Cho, B. Brettmann, W.R. Gutekunst, R. Ramprasad, H.J. Qi, Chemical circularity in 3D printing with biobased Δ-valerolactone, Adv. Mater. 2310040 (2024) 1–8, https://doi.org/10.1002/adma.202310040.

[34] L. Li, H. Liu, Y. Zhao, X. Liu, Y. Dong, J. Luo, X. Jiang, Y. Zhang, Q. Zhu, X. Yuan, X. Pei, L. Zhang, B. Li, S. Yang, M. Gou, 3D printing of maturable tissue constructs using a cell-adaptable nanocolloidal hydrogel, Adv. Funct. Mater. 2402341 (2024) 1–14, https://doi.org/10.1002/adfm.202402341.

[35] S.S. Lee, N. Kleger, G.A. Kuhn, H. Greutert, X. Du, T. Smit, A.R. Studart, S. J. Ferguson, A 3D-printed assemblable bespoke scaffold as a versatile microcryogel carrier for site-specific regenerative medicine, Adv. Mater. 35 (2023), https://doi.org/10.1002/adma.202302008.

[36] A. Ron, E.U. Azeloglu, R.C. Calizo, M. Hu, S. Bhattacharya, Y. Chen, G. Jayaraman, S. Lee, S.R. Neves-Zaph, H. Li, R.E. Gordon, J.C. He, J.C. Hone, R. Iyengar, Cell shape information is transduced through tension-independent mechanisms, Nat. Commun. 8 (2017) 2145, https://doi.org/10.1038/s41467-017-02218-4.

[37] J. Kim, H. Lee, G. Lee, D. Ryu, G. Kim, Fabrication of fully aligned self-assembled cell-laden collagen filaments for tissue engineering via a hybrid bioprinting process, Bioact. Mater. 36 (2024) 14–29, https://doi.org/10.1016/j.bioactmat.2024.02.020.

[38] X. Xu, H. Li, J. Chen, C. Lv, W. He, X. Zhang, Q. Feng, H. Dong, A universal strategy to construct high-performance homo- and heterogeneous microgel assembly bioinks, Small Methods 2400223 (2024) 1–14, https://doi.org/10.1002/smtd.202400223.

[39] B. Kong, Y. Chen, R. Liu, X. Liu, C. Liu, Z. Shao, L. Xiong, X. Liu, W. Sun, S. Mi, Fiber reinforced GelMA hydrogel to induce the regeneration of corneal stroma, Nat. Commun. 11 (2020) 1435, https://doi.org/10.1038/s41467-020-14887-9.

[40] L. Ouyang, J.P.K. Armstrong, Y. Lin, J.P. Wojciechowski, C. Lee-Reeves, D. Hachim, K. Zhou, J.A. Burdick, M.M. Stevens, Expanding and optimizing 3D bioprinting capabilities using complementary network bioinks, Sci. Adv. 6 (2020) 1–14, https://doi.org/10.1126/sciadv.abc5529.

[41] G. Tang, Z. Luo, L. Lian, J. Guo, S. Maharjan, C.E. Garciamendez-Mijares, M. Wang, W. Li, Z. Zhang, D. Wang, M. Xie, H. Ravanbakhsh, C. Zhou, X. Kuang, Y. Hou, X. Yu, Y.S. Zhang, Liquid-embedded (bio)printing of alginate-free, standalone, ultrafine, and ultrathin-walled cannular structures, Proc. Natl. Acad. Sci. USA 120 (2023) 2017, https://doi.org/10.1073/pnas.2206762120.

[42] M. Wang, W. Li, J. Hao, A. Gonzales, Z. Zhao, R.S. Flores, X. Kuang, X. Mu, T. Ching, G. Tang, Z. Luo, C.E. Garciamendez-Mijares, J.K. Sahoo, M.F. Wells, G. Niu, P. Agrawal, A. Quiñones-Hinojosa, K. Eggan, Y.S. Zhang, Molecularly cleavable bioinks facilitate high-performance digital light processing-based bioprinting of functional volumetric soft tissues, Nat. Commun. 13 (2022) 3317, https://doi.org/10.1038/s41467-022-31002-2.

[43] H. Ravanbakhsh, Z. Luo, X. Zhang, S. Maharjan, H.S. Mirkarimi, G. Tang, C. Chávez-Madero, L. Mongeau, Y.S. Zhang, Freeform cell-laden cryobioprinting for shelf-ready tissue fabrication and storage, Matter 5 (2022) 573–593, https://doi.org/10.1016/j.matt.2021.11.020.

[44] A. Lee, A.R. Hudson, D.J. Shiwarski, J.W. Tashman, T.J. Hinton, S. Yerneni, J. M. Bliley, P.G. Campbell, A.W. Feinberg, 3D bioprinting of collagen to rebuild components of the human heart, Science 365 (2019) 482–487, https://doi.org/10.1126/science.aav9051 (80-.).

[45] Q. Wang, Ö. Karadas, J.M. Rosenholm, C. Xu, T. Näreoja, X. Wang, Bioprinting macroporous hydrogel with aqueous two-phase emulsion-based bioink: in vitro mineralization and differentiation empowered by phosphorylated cellulose nanofibrils, Adv. Funct. Mater. 2400431 (2024) 1–17, https://doi.org/10.1002/adfm.202400431.

[46] G. Ying, N. Jiang, S. Maharjan, Y. Yin, R. Chai, X. Cao, J. Yang, A.K. Miri, S. Hassan, Y.S. Zhang, Aqueous two-phase emulsion bioink-enabled 3D bioprinting of porous hydrogels, Adv. Mater. 30 (2018) 1805460, https://doi.org/10.1002/adma.201805460.

[47] Z. Chen, Z. Lv, Y. Zhuang, Q. Saiding, W. Yang, W. Xiong, Z. Zhang, H. Chen, W. Cui, Y. Zhang, Mechanical signal-tailored hydrogel microspheres recruit and train stem cells for precise differentiation, Adv. Mater. 35 (2023) e2300180, https://doi.org/10.1002/adma.202300180.

[48] J. Tao, S. Zhu, N. Zhou, Y. Wang, H. Wan, L. Zhang, Y. Tang, Y. Pan, Y. Yang, J. Zhang, R. Liu, Nanoparticle-stabilized emulsion bioink for digital light processing based 3D bioprinting of porous tissue constructs, Adv. Healthcare Mater. 11 (2022) 1–27, https://doi.org/10.1002/adhm.202102810.

[49] M. Lian, B. Sun, Y. Han, B. Yu, W. Xin, R. Xu, B. Ni, W. Jiang, Y. Hao, X. Zhang, Y. Shen, Z. Qiao, K. Dai, A low-temperature-printed hierarchical porous sponge-like scaffold that promotes cell-material interaction and modulates paracrine activity of MSCs for vascularized bone regeneration, Biomaterials 274 (2021) 120841, https://doi.org/10.1016/j.biomaterials.2021.120841.

[50] L. Zhou, Z. Zeng, S. Liu, T. Min, W. Zhang, X. Bian, H. Du, P. Zhang, Y. Wen, Multifunctional DNA hydrogel enhances stemness of adipose-derived stem cells to activate immune pathways for guidance Burn wound regeneration, Adv. Funct. Mater. 32 (2022), https://doi.org/10.1002/adfm.202207466.

[51] J. Beumer, H. Clevers, Hallmarks of stemness in mammalian tissues, Cell Stem Cell 31 (2024) 7–24, https://doi.org/10.1016/j.stem.2023.12.006.

[52] C. Zhao, K. Lin, X. Wang, Maintenance and modulation of stem cells stemness based on biomaterial designing via chemical and physical signals, Appl. Mater. Today 19 (2020) 100614, https://doi.org/10.1016/j.apmt.2020.100614.

[53] Y. Xu, Y. Zhang, J.C. García-Cañaveras, L. Guo, M. Kan, S. Yu, I.A. Blair, J. D. Rabinowitz, X. Yang, Chaperone-mediated autophagy regulates the pluripotency of embryonic stem cells, Science 369 (2020) 397–403, https://doi.org/10.1126/science.abb4467 (80-.).

[54] X. He, Y. Zhu, L. Yang, Z. Wang, Z. Wang, J. Feng, X. Wen, L. Cheng, R. Zhu, MgFe-LDH nanoparticles: a promising leukemia inhibitory factor replacement for self-renewal and pluripotency maintenance in cultured mouse embryonic stem cells, Adv. Sci. 8 (2021) 1–14, https://doi.org/10.1002/advs.202003535.

[55] L. Chen, M. Carlton, X. Chen, N. Kaur, H. Ryan, T.J. Parker, Z. Lin, Y. Xiao, Y. Zhou, Effect of fibronectin, FGF-2, and BMP4 in the stemness maintenance of BMSCs and the metabolic and proteomic cues involved, Stem Cell Res. Ther. 12 (2021) 1–13, https://doi.org/10.1186/s13287-021-02227-7.

[56] Y.W. Eom, J.E. Oh, J.I. Lee, S.K. Baik, K.J. Rhee, H.C. Shin, Y.M. Kim, C.M. Ahn, J. H. Kong, H.S. Kim, K.Y. Shim, The role of growth factors in maintenance of stemness in bone marrow-derived mesenchymal stem cells, Biochem. Biophys. Res. Commun. 445 (2014) 16–22, https://doi.org/10.1016/j.bbrc.2014.01.084.

[57] A.A.K. Das, B.W. Filby, D.A. Geddes, D. Legrande, V.N. Paunov, High throughput fabrication of cell spheroids by templating water-in-water Pickering emulsions, Mater. Horiz. 4 (2017) 1196–1200, https://doi.org/10.1039/c7mh00677b.

[58] H. Xiang, C. Zhang, Y. Xiong, Y. Wang, C. Pu, J. He, L. Chen, K. Jiang, W. Zhao, H. Yang, F. Wang, Y. Li, MMP13-responsive hydrogel microspheres for

osteoarthritis treatment by precise delivery of celecoxib, Mater. Des. 241 (2024) 112966, https://doi.org/10.1016/j.matdes.2024.112966.